Journal of Ovonic Research Vol. 21, No. 5, September - October 2025, p. 643 - 656

Enhancing the efficiency of lead-free $Cs_2BiAgBr_6$ double perovskite solar cells

F. Otmani [*], K. Youbi, F. Fatmi Frid, S. Bensenouci
Unity of Research of Materials and Renewable Energies (URMER), University of Tlemcen BP: 119 Tlemcen 13000 Algeria

In the present research, the photovoltaic performance of a lead-free double perovskite photovoltaic cell using $Cs_2AgBiBr_6$ as the active layer was systematically investigated through numerical simulation using OghmaNano software. The device structure considered was FTO/TiO_2/$Cs_2AgBiBr_6$/Spiro-OMeTAD/Au. The study focused on optimizing the physical and electrical parameters, including the thickness of each layer, doping concentration, and series resistance, to enhance device efficiency.

The optimal device performance was achieved when the active layer thickness was set to 500 nm, combined with well-tuned transport layers and favorable electrical conditions. Under illumination conditions of AM1.5G (1000 W/m²) at 300 K, the optimized device achieved a short-circuit current density (Jsc) of 7.97 mA/cm², an open-circuit voltage (Voc) of 0.988 Volts, a fill factor (FF) of 86.52%, and a power conversion efficiency (PCE) of 6.81%**.** The findings suggest the promise of $Cs_2AgBiBr_6$ as a sustainable and environmentally friendly substitute for perovskites containing lead. Nonetheless, the limited of light absorption in the near-infrared (NIR) spectrum suggests a need for advanced light management strategies. Future developments may include the integration of tandem architectures to further improve spectral utilization and device efficiency.

(Received July 5, 2025; Accepted October 9, 2025)

Keywords: Perovskites solar cell, $Cs_2BiAgBr_6$, Conversion efficiency,
OghmaNano software, Thickness, Temperature

1. Introduction

In recent times, mixed organic–inorganic perovskite solar cells (HPSCs) have garnered substantial interest owing to their outstanding intrinsic characteristics, notably low manufacturing costs, high charge carrier mobility's, adjustable bandgap, extended carrier diffusion lengths, and excellent light absorption capabilities [1-2].

The perovskite crystal structure is characterized by a general formula of ABX_3, in this configuration: A present a larger cation (usually an organic or inorganic ion) for example methylammonium (MA) or formamidinium (FA) molecule positively charged ($CH_3NH_3^+$ MA^+) or NH_2CHNH_2 $^+(FA^+)$), B represents a divalent metal cation, including (Pb_2^+, Sn_2^+, Ge_2^+) and **X** is a halogen/anions (typically iodide I^-, bromide Br^-, chloride Cl^-) [3].

Perovskite solar cells (PSCs) have seen a significant improvement in their power conversion efficiency (PCE), ranging between 3.8% and 26.1% for single-junction devices and reaching up to 29.1% for multi-junction configurations as of 2023 [4-5].

Nonetheless, lead-based organic–inorganic halide perovskites pose environmental and health concerns due to the inclusion of lead along with volatile organic cation (MA^+ and FA^+), which tend to undergo spontaneous decomposition, even in the absence of external stimuli. [6-7].

In this context, the quest for perovskite materials that combine stability, non-toxicity, and high efficiency remains a major challenge. Recently, double perovskites with the general formula $A_2B^+B'^{3+}X_6$ have attracted growing interest from the research community [8-9].

Several lead-free double perovskite structures have been examined as viable alternatives to conventional lead-based materials, including, $Cs_2AgInCl_6$ [10], Cu_2AgBiI_6 [11], Cs_2NaBiI_6 [12], and Cs_2AgBiX_6 (X = I, Cl, Br) [13] each exhibiting different levels of photovoltaic performance. Among these, $Cs_2BiAgBr_6$ has attracted particular interest due to its lead-free composition, superior

---

[*] Corresponding author: fatimazohra.otmani@univ-tlemcen.dz

https://doi.org/10.15251/JOR.2025.215.643

environmental stability, and advantageous optoelectronic characteristics, which position it as a promising candidate for photovoltaic applications.

As depicted in Fig. 1, the composition of the lead-free double perovskite $Cs_2BiAgBr_6$ includes cesium, silver, bismuth, and bromine elements. The crystalline configuration of the compounds consists of corner-sharing $[AgBr_6]^{5-}$ and $[BiBr_6]^{3-}$ octahedra, with Cs^+ cations occupying the A-site positions in the lattice. According to X-ray diffraction analysis, this substance crystallizes in a cubic phase with a space group of $Fm\bar{3}m$ and a lattice parameter of a 11. 27 Å [14]. An indirect electronic band gap in the vicinity of 2 eV has also been reported, making it a suitable candidate for photovoltaic applications because of its strong light absorption across the visible region [15].

Designing efficient photovoltaic devices requires a thorough understanding of the electronic and physical properties of the materials involved in the solar cell structure. In this context, transparent conductive oxides like FTO, electron transport layers such as TiO_2, and hole transport materials like Spiro-OMeTAD are key components that govern charge extraction, transport behavior, and recombination processes.

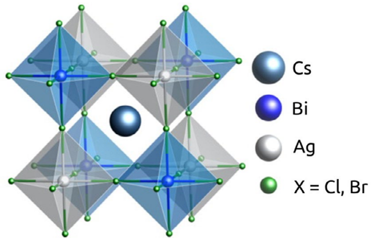

Fig.1. Double perovskite structure [16-17].

This study presents a theoretical simulation of a $Cs_2BiAgBr_6$ based perovskite solar cell using the OghmaNano software. The simulation focuses on optimizing the device structure and evaluating its performance based on key physical parameters, namely band energy gap, electronic affinity, carrier transport characteristics, density of states and dielectric property.

2. Device structure and theoretical simulation

The analysis of semiconductors is primarily based on a set of fundamental equations, commonly referred to as "transport equations." Solving these equations makes it possible to describe various physical phenomena such as recombination or defects in solar photovoltaic devices. In fact, the simulation of photovoltaic cells, particularly those made of Perovskites materials (PCS) is crucial for optimizing device performance. Moreover, the use of solar simulators has become an essential tool for the design and analysis of solar cells. The OghmaNano simulation software was employed as a potent instrument for device modeling and examination in our work. This simulator includes the Shockley-Read-Hall (SRH) formalism to account for carrier recombination and trap-assisted transitions phenomena, alongside a drift-diffusion framework. It also numerically resolves Poisson's, and carrier continuity equations, thus enabling a detailed understanding of the optoelectronic response of the device [18-19].

$$\frac{d}{dx}\varepsilon_0\varepsilon_r = \frac{\partial\varphi}{\partial x} = q(n-p) \tag{1}$$

$$J_n = q\mu_c n\frac{\partial E_c}{\partial x} + qD_n\frac{\partial n}{\partial x} \tag{2}$$

$$J_p = q\mu_n p\frac{\partial E_v}{\partial x} + qD_p\frac{\partial p}{\partial x} \tag{3}$$

$$\frac{\partial J_n}{\partial x} = q\left(R_n - G + \frac{\partial p}{\partial x}\right) \tag{4}$$

$$\frac{\partial J_p}{\partial x} = -q\left(R_n - G + \frac{\partial p}{\partial x}\right) \tag{5}$$

Fig. 2 illustrates Device structure used in the numerical simulation of the $Cs_2BiAgBr_6$ Perovskites solar cell. However, the simulated device in this study adopts the following layer configuration: FTO/TiO_2/$Cs_2BiAgBr_6$/Spiro-OMeTAD/Au. Tables 1 and 2 summarize the key physical parameters of the active layer and the other materials employed in the simulation, respectively.

Fig. 2. Schematic of the planar heterojunction architecture of a typical perovskite-based device

Table 1. Key physical parameters of the $Cs_2AgBiBr_6$ active layer employed in the numerical simulation.

Parameters (Symbol)	Values
N_c (m^{-3})	1×10^{26}
N_v (m^{-3})	1×10^{26}
$N_{t,e}$ (m^{-3} eV^{-3})	1×10^{20}
$N_{t,h}$ (m^{-3} eV^{-3})	1×10^{20}
$\sigma_{et\rightarrow h}$ (m^{-2})	1×10^{-22}
$\sigma_{ht\rightarrow e}$ (m^{-2})	1×10^{-22}
$\sigma_{e\rightarrow et}$ (m^{-2})	1×10^{-20}
$\sigma_{h\rightarrow ht}$ (m^{-2})	1×10^{-20}
$E_{t,e}$ (eV)	0.06
$E_{t,h}$ (eV)	0.06
μ_e (cm^2 /Vs)	0.37
μ_h (cm^2 /Vs)	0.37
Eg (eV)	1.9
χ (eV)	3.79
ε_r (au)	5.80
τ_e (s)	1.75×10^{-8}
τ_e (s)	1.75×10^{-8}
References	[20-21]

Table 2. Key physical parameters of the various materials employed in the simulation.

	FTO	TiO_2	Spiro-OMeTAD
Eg (eV)	3.5	3.26	3
χ (eV) (eV)	4.5	4.20	2.45
ε_r (au)	10	10	3
μ_e (cm^2/ Vs)	100	100	2×10^{-4}
μ_h (cm^2 /Vs)	20	25	2×10^{-4}
N_c (cm^{-3})	2.2×10^{18}	2×10^{17}	2.2×10^{18}
N_v (cm^{-3})	2.2×10^{18}	6×10^{18}	1.9×10^{19}
References	[22-23]	[24-25]	[26]

The main goal of the simulation was to optimize the thickness of the $Cs_2AgBiBr_6$ absorber and assess its influence on the principal photovoltaic performance metrics, including: open-circuit voltage (Voc), short-circuit current density (Jsc), fill factor (FF), and power conversion efficiency (PCE). Additional simulations were also performed to study the device response under temperature variations and to analyze the EQE spectra. Simulations were conducted under standard AM1.5G solar illumination conditions at 300 K, incorporating a series resistance of 19.5 Ω.

3. Results and discussion

Initially, our simulation focused on studying the impact of tuning the thicknesses of the various material layers on the electrical output characteristics of the device. Subsequently, we have evaluated the effect of various materials used as back electrodes, including gold (Au), silver (Ag), and aluminum (Al). We have also analyzed the influence of temperature, active layer doping, and series resistance. Finally, an optical simulation was carried out to complement the study.

3.1. Impact of active layer thickness variation on device performance

Fig. 3 shows the impact of the active layer thickness ($Cs_2BiAgBr_6$) on the photovoltaic properties of the FTO/TiO_2/$Cs_2BiAgBr_6$/Spiro-OMeTAD/Au solar cell. As illustrated in Fig.3.a, Voc increases steadily with thickness and begins to saturate beyond ~600 nm, which can be attributed to enhanced light absorption and a higher quasi-Fermi level splitting [27]. According to Fig. 3b, Jsc exhibits a distinct peak at approximately 500 nm. This behavior is typical of a trade-off between increased photon absorption at greater thicknesses and enhanced recombination losses due to longer carrier transport paths. Similarly, FF (Fig. 3c) reaches a maximum near 650 nm and then decreases, likely Attributed to the rising series resistance (Rs) and increased recombination in thicker layers. As a consequence, PCE exhibits an optimal value at around 500 nm, beyond which the efficiency declines (Fig. 3d). These findings highlight the role of active layer thickness optimization to balance photon absorption and charge collection for improved device performance [28].

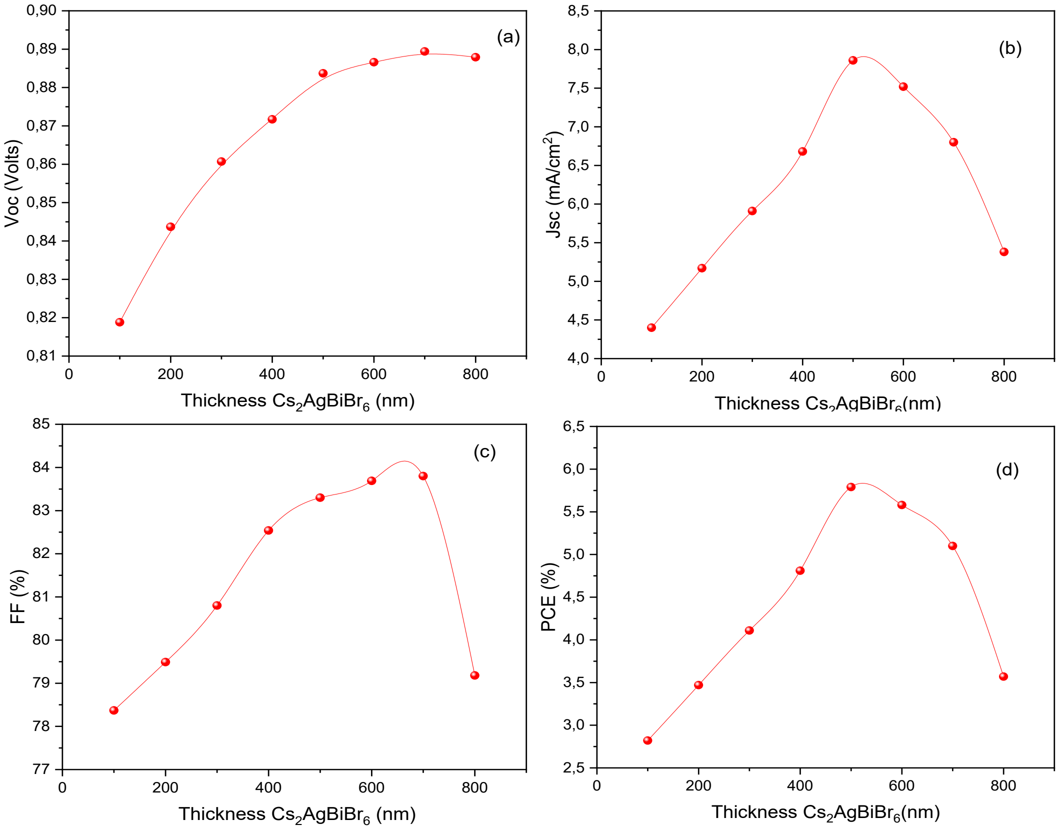

Fig. 3. (a, b, c, d). Effect of active layer thickness on device photovoltaic performance: a) Voc, b) Jsc, c) FF, and d) PCE.

3.2. Influence of FTO, TiO_2, and Spiro-OMeTAD thickness on PCE

Fig. 4 presents the influence of varying the thickness of three critical layers FTO, TiO_2, and Spiro-OMeTAD on PCE of the device.

Fig. 4.a shows that the PCE remains relatively stable for FTO thicknesses in the range of 20–50 nm, but begins to decline sharply beyond 70 nm. This trend can be attributed to the increased series resistance associated with thicker FTO layers, which limits current flow and introduces ohmic losses. Additionally, thicker FTO layers can reduce optical transmittance, thereby decreasing the amount of light reaching the active layer. An optimal FTO thickness around 50 nm ensures sufficient conductivity and transparency [29].

In Fig.4.b, the PCE increases with TiO_2 thickness, reaching a peak near 200 nm, and then gradually decreases. TiO_2 acts as the electron transporting-layer (ETL), and its role appears crucial for efficiently extracting photogenerated electrons while preventing direct contact between the FTO and the perovskite, which could lead to shunting. However, excessively thick TiO_2 layers introduce higher resistance to electron transport and can act as recombination centers, thereby reducing charge extraction efficiency [30].

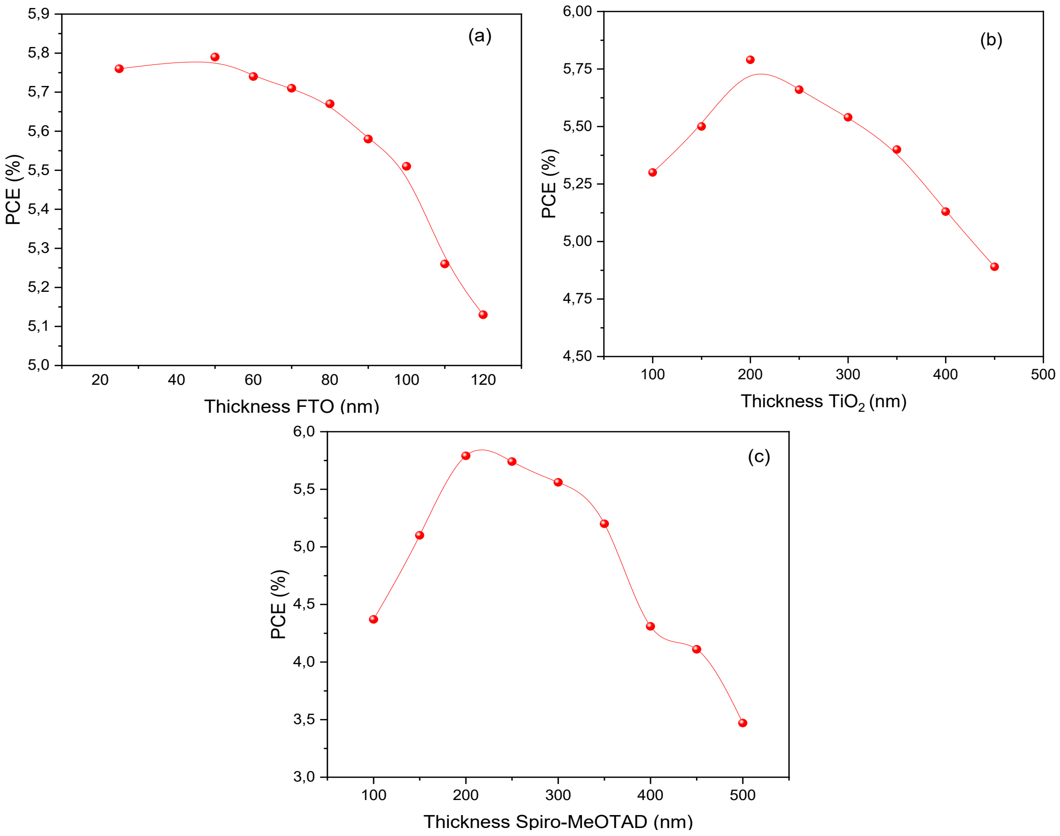

Fig. 4. (a, b, c). Impact of layer thickness on PCE FTO, b) TiO_2 *and c) spiro-MeOTAD.*

Fig. 4.c illustrates Spiro-OMeTAD serving as the hole transporting-layer (HTL), also exhibits an optimal thickness around 250 nm. Below this value, incomplete coverage of the perovskite layer may lead to inefficient hole collection and interfacial recombination. Conversely, when the HTL becomes too thick, the increased series resistance and additional optical losses due to absorption in the Spiro-OMeTAD diminish overall device efficiency **[30].**

These results underscore the significance of precisely optimizing the thickness of each layer in the device architecture. The best performance is achieved by balancing electrical conductivity, charge transport/extraction, and optical transparency factors that are strongly dependent on the individual layer thicknesses.

3.3. Effect of back electrode material on device performance

Table 3 summarizes the impact of different back electrode materials (Au, Ag, and Al) on parameters of performance of the simulated device with the structure FTO/TiO_2/$Cs_2BiAgBr_6$/Spiro-OMeTAD/Metal. The variation in photovoltaic parameters is relatively small, indicating that the performance of the device is highly insensitive to the choice of electrode within the tested materials.

Voc shows minimal change, ranging from 0.8837 V with Au to 0.8840 V with both Ag and Al. A slight raise in Jsc is observed for Ag and Al (7.94 mA/cm^2) compared to Au (7.86 mA/cm^2). Likewise, the FF improves marginally ranging from 83.30% (Au) to 83.36% (Ag and Al). Consequently, the PCE increases from 5.79% with Au to 5.85% when Ag or Al is used.

These results suggest that Ag and Al are promising low-cost alternatives to Au, offering comparable or slightly improved photovoltaic performance. This substitution can contribute to reducing fabrication costs while maintaining device efficiency, which is particularly valuable for large-scale deployment of lead-free perovskite photovoltaic devices.

Table 3. Effect of different electrode on the device performance characteristics.

	Voc (Volts)	Jsc (mA/cm^2)	FF (%)	PCE (%)
Au	0.8837	7.86	83.30	5.79
Ag	0.8840	7.94	83.36	5.85
Al	0.8840	7.94	83.36	5.85

3.4. Impact of temperature on device performance

Fig.5 illustrates the impact of temperature on the electrical performance parameters of the perovskite device structured as FTO/TiO_2/$Cs_2BiAgBr_6$/Spiro-OMeTAD/Au. According in Fig.5.a, a nearly linear decrease in Voc is observed with a rise in temperature. This decline is primarily attributed to enhanced non-radiative recombination processes, reduced charge carrier mobility, and a decrease in the effective band gap at elevated temperatures. Such behavior is characteristic of solar cells, where high temperatures lead to gradual performance degradation [31].

Although the short-circuit current density (Jsc) remains relatively stable across the studied temperature range (300–360 K), a slight increase can be noticed at the beginning, likely due to increased charge carrier generation. However, this improvement is minimal compared to the detrimental effect of temperature on Voc.

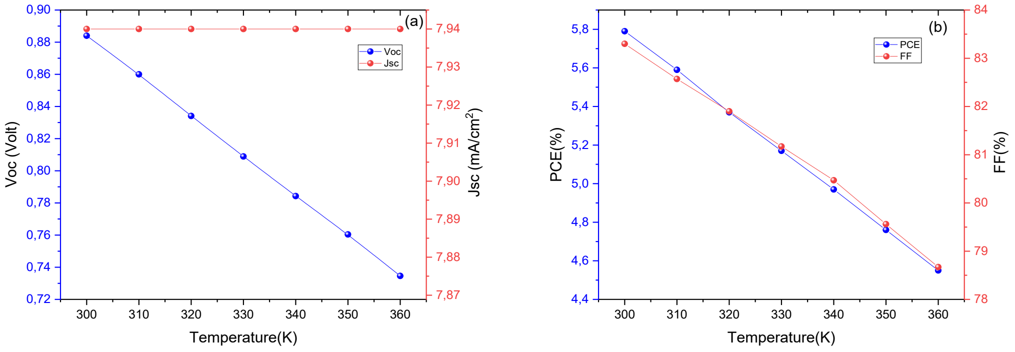

Fig. 5. (a, b). Influence of temperature a) Voc and Jsc, b) FF and PCE.

Fig.5.b shows that both the FF and PCE decline steadily with increasing temperature. These reductions are mainly the result of increased resistive losses (higher series resistance), reduced shunt resistance, and the drop in Voc. The thermal effects degrade the junction quality and hinder charge collection, thereby limiting the output power of the device.

In summary, increasing temperature negatively impacts key PV parameters especially Voc, FF, and PCE thereby reducing the cell's power conversion efficiency. This analysis highlights the importance of thermal stability for the development of efficient, lead-free perovskite-based photovoltaic cells, particularly for real-world operational conditions [29].

Furthermore, the characteristic shape of the J–V curve degrades with temperature, indicating increased series resistance and reduced diode quality, as shown in Fig.6. The knee of the curve, where maximum power is extracted, shifts downward and toward lower voltages as the temperature rises, reflecting a decline in both the FF and PCE.

The present analysis confirms that thermal effects significantly impair the photovoltaic performance, underlining the importance of developing thermally stable materials and device architectures for sustainable and efficient solar energy harvesting [32].

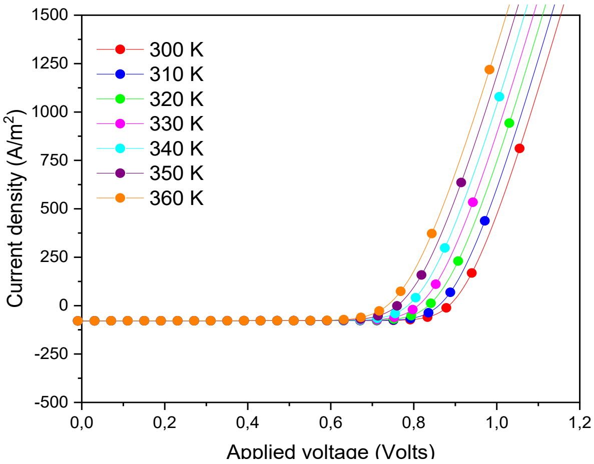

Fig. 6. Current density – voltage (J-V) at different temperature.

3.5. Impact of $Cs_2BiAgBr_6$ doping concentration on solar cell performance

Table 4 and Fig. 7 illustrate the impact of varying the donor doping level the effect of varying donor doping concentration (Nd) in the $Cs_2BiAgBr_6$ absorber layer on characteristics of PCS. The results show that for doping levels ranging from 10^{14} to 10^{20} cm^{-3}, the solar cell characteristics (Jsc, Voc, FF and PCE), remain constant, indicating a stable electrical response in this doping regime.

However, beyond a critical threshold of Nd=10^{22} cm^{-3}, a slight decline in FF and Jsc is noticed, and for Nd=10^{24} cm^{-3}, the device exhibits a drastic drop in performance, with the Jsc decreasing from 7.96 to 5.73 mA/cm², the FF falling from 86.13% to 76.73%, and the PCE dropping significantly from 6.78% to 4.33%. This deterioration is ascribed to enhanced non-radiative recombination mechanisms and increased carrier scattering at high doping levels, which impair charge transport and collection [29-30].

These findings suggest that moderate doping levels (up to 10^{20} cm^{-3}) are favorable for optimal device performance, while excessive doping concentrations degrade the photovoltaic efficiency by affecting the internal electric field and increasing recombination losses.

Table 4. Solar cell parameters for different $Cs_2BiAgBr_6$ doping variation (Nd).

Nd (cm^{-3})	J_{SC} (mA/cm^2)	V_{oc}(volt)	FF (%)	PCE (%)
1×10^{14}	7,96	0,988	86,13	6,78
1×10^{16}	7,96	0,988	86,13	6,78
1×10^{18}	7,96	0,988	86,13	6,78
1×10^{20}	7,96	0,988	86,13	6,78
1×10^{22}	7,94	0,988	85,69	6,73
1×10^{24}	5,73	0,984	76,73	4,33

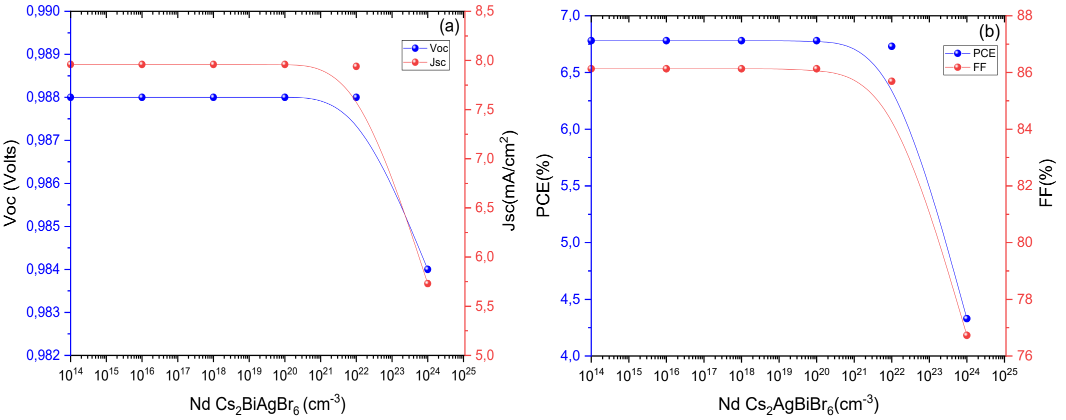

Fig. 7. (a, b). Effect of $Cs_2BiAgBr_6$ doping concentration (Nd) on (a) Jsc and Voc, (b) PCE and FF.

3.6. Impact of Rs on solar cell performance

Table data highlights the impact of varying Rs on the electrical characteristic of a device based on $Cs_2BiAgBr_6$ as an absorber material. As Rs declines from 25.5 Ω to 10.5 Ω, FF slightly improves from 85.88% to 86.52%, resulting in a modest rise in PCE from 6.76% to 6.81%.

Voc remains constant at a value of 0.988 Volts, and the Jsc shows minimal variation, indicating that Rs primarily affects the FF through ohmic losses. Lower series resistance reduces internal voltage drops, thereby enhancing carrier extraction and overall device efficiency.

These results emphasize the importance of minimizing series resistance to optimize the efficiency of lead-free $Cs_2BiAgBr_6$ based photovoltaic cells, ensuring effective carrier transfer and collection within the device architecture.

Table 5. Solar cell parameters for different series resistance **(**Rs**)**

Rs (Ω)	**J_{SC} (mA/cm^2)**	**Voc (volt)**	**FF (%)**	**PCE (%)**
25.5	7,96	0,988	85,88	6,76
19.5	7,96	0,988	86,13	6,78
15.5	7,96	0,988	86,30	6,80
10.5	7,97	0,988	86,52	6,81

3.7. EQE spectra of the FTO/TiO_2/ $Cs_2AgBiBr_6$ /Spiro/Ag solar cell

EQE spectrum of the simulated perovskite solar cell based on the $Cs_2BiAgBr_6$ absorber material is depicted in Fig.8. EQE represents the fraction of incident photons converted into electrons at each wavelength and is a key indicator of the photoresponse of the device across the solar spectrum.

The EQE curve shows a broad response extending from approximately 300 nm to 750 nm, with peak conversion efficiency evident in the visible range between 350 nm and 500 nm, where EQE values exceed 70%. This indicates that the $Cs_2BiAgBr_6$ absorber material is particularly effective at harvesting visible light.

However, the EQE starts to decline beyond 500 nm, dropping significantly in the near-infrared (NIR) range, revealing a limitation in the absorption range of the material due to its relatively wide bandgap. The sharp drop in EQE below 320 nm is attributed to parasitic absorption or reflection losses in the front contact layers (FTO or TiO_2).

Overall, the EQE spectrum confirms the potential of $Cs_2BiAgBr_6$ for visible light harvesting but also highlights the need for improvement in the near-infrared response, possibly through the use of tandem configurations or bandgap engineering to extend the absorption range and improve current generation.

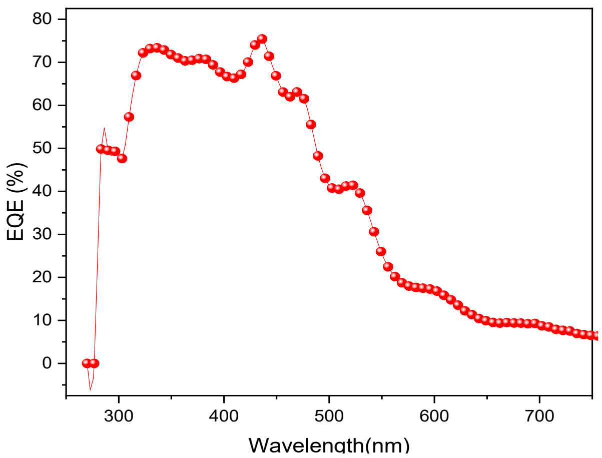

Fig. 8. EQE response of FTO/TiO₂/ Cs₂BiAgBr₆/ Spiro-MeOTAD /Ag structures.

3.8. Optical simulation analysis of the $Cs_2AgBiBr_6$ based solar cell

3.8.1. Energy band alignment and photogeneration rate profile

An optical simulation was carried out to investigate the photogeneration profile and energy band alignment within a solar cell structure incorporating $Cs_2AgBiBr_6$ as the photoactive material. The simulated device architecture consists of the following layers:

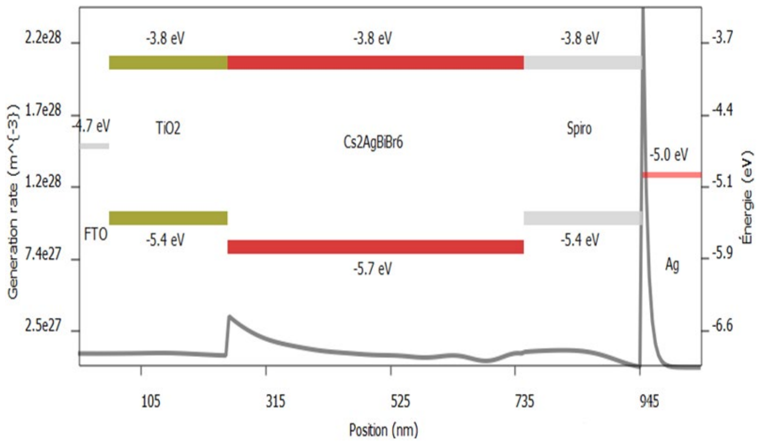

Fig. 9. Simulated energy band alignment and photogeneration rate profile of the FTO/TiO₂/ Cs₂AgBiBr₆/Spiro/Ag solar cell.

FTO/TiO_2/ $Cs_2AgBiBr_6$ /Spiro-OMeTAD/Ag. The generation rate profile clearly indicates that photon absorption and hence carrier generation is predominantly confined within the $Cs_2AgBiBr_6$ layer, which is consistent with its function as the main light-harvesting material. The other layers, including TiO_2, Spiro-OMeTAD, and the contact electrodes (FTO and Ag), contribute minimally to the generation rate, reflecting their transparency or low absorption in the relevant spectral range.

The energy level diagram demonstrates a favorable band alignment across the device.

The conduction band edge (BC) of TiO_2 (–3.8 eV) aligns well with the corresponding level in $Cs_2AgBiBr_6$, enabling efficient electron extraction. Similarly, the valence band maximum (VBM) of Spiro-OMeTAD (-5.4 eV) is suitably positioned relative to that of $Cs_2AgBiBr_6$ (-5.7 eV), facilitating effective hole transport as shown in Fig.9. This energy configuration supports selective carrier extraction and minimizes nonradiative recombination at the interfaces.

These results suggest that, although $Cs_2AgBiBr_6$ possesses an indirect band gap, careful optimization of interface properties and the design of charge-transport layers can greatly improve carrier extraction, highlighting its potential as a stable, lead-free perovskite solar cell material.

3.8.2. Analysis of photon and absorbed photon densities

To better understand the light matter interaction within the device, two-dimensional optical simulations were performed to evaluate the photon density and the absorbed photon density as functions of both wavelength and position along the device thickness.

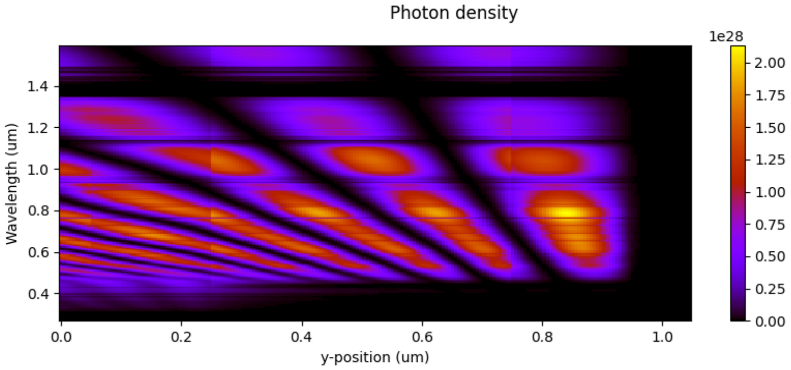

Fig. 10. Spectral distributions of incident photons.

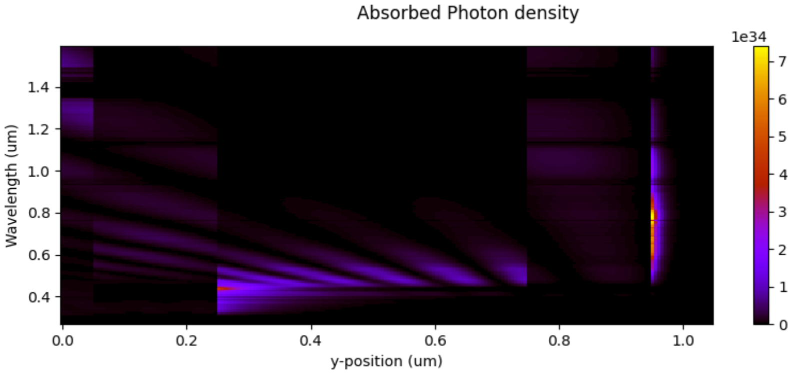

Fig. 11. Spectral distributions of absorbed photons.

Fig.10 and Fig.11 show the photon density and the absorbed photon density across the structure respectively. In contrast, the absorbed photon density is mostly localized within the photoactive $Cs_2AgBiBr_6$ layer, and is concentrated at wavelengths below 600 nm. This indicates that the material has limited absorption in the near-infrared region, likely because of its indirect bandgap energy and relatively low optical absorption coefficient at longer wavelengths. As a result, a considerable portion of incident light, especially in the infrared, remains unutilized.

To overcome this limitation, integrating the device into a tandem architecture offers a promising solution. For instance, pairing the $Cs_2AgBiBr_6$ top cell with a lower cell made of silicon (or another narrow band gap absorber) can extend the spectral coverage and more effectively harness low-energy photons. Tandem solar cells are specifically designed to reduce transmission losses and improve the overall quantum efficiency, thus boosting the power conversion efficiency.

These findings highlight the importance of advanced optical design in combination with tandem device architectures to mitigate spectral absorption losses and fully exploit the solar spectrum in lead free perovskite-based systems [33].

3.9. Device optimization and photovoltaic performance

Following a comprehensive series of simulations, an optimized configuration of the $Cs_2AgBiBr_6$ based photovoltaic cell was established to improve overall device performance. The optimal layer thicknesses were determined as follows: FTO (50 nm)/TiO_2 (200 nm)/ $Cs_2AgBiBr_6$ (500 nm)/Spiro-OMeTAD (200 nm)/ Ag (100 nm). Additionally, a doping concentration of $1\times10^{20}cm^{-3}$ was applied to the transport layers, along with a series resistance of 10.5 Ω to realistically represent contact and bulk resistive effects. Fig.12 presents the simulated J–V characteristic for the optimized device configuration, under standard test conditions (AM1.5G, 1000 W/m²) and temperature (300 K). The device exhibits the following key performance parameters: Jsc of 7.97 mA/cm², Voc of 0.988 V, FF of 86.52%**,** and PCE of 6.81%.

These results demonstrate that the optimized device advantages from efficient charge carrier transport and minimized recombination losses, as reflected in the high fill factor and voltage. The absorber thickness of 500 nm enables sufficient light absorption in the visible range, while the appropriately engineered transport layers facilitate effective carrier extraction. However, the relatively modest Jsc indicates that the optical absorption of $Cs_2AgBiBr_6$ remains a limiting factor especially in the near infrared region suggesting that further improvement could be achieved through light trapping techniques or the implementation of tandem solar cell architectures.

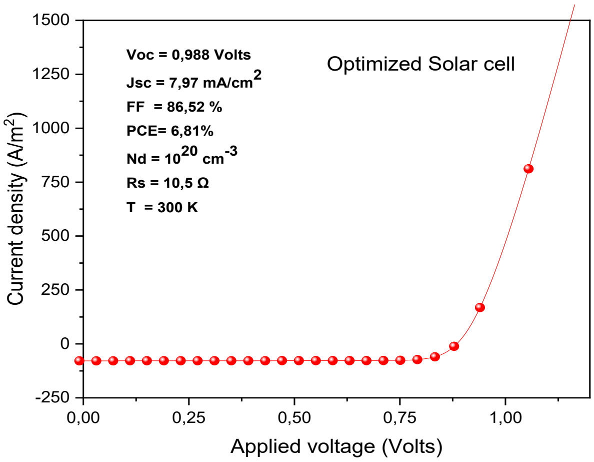

Fig. 12. J–V characteristics of the optimized solar cell structure.

3.10. Comparison with reported literature

Table 6 presents a comparison of the performance of the considered $Cs_2AgBiBr_6$ based perovskite photovoltaic cell with previously reported devices.

The results from the comparison provide clear evidence that the effectiveness of the proposed device architecture. With FF of 86.52% and PCE of 6.81%, the optimized structure surpasses most previously reported configurations, highlighting its potential for improved charge extraction and reduced recombination losses in lead-free perovskite cells.

Table 6. Comparison of proposed model with previously published results.

	Jsc (mA/cm²)	**Voc (volts)**	**FF (%)**	**PCE (%)**
ITO/SnO_2/ $Cs_2AgBiBr_6$/P3HT/Ag [34]	3.15	0.95	68.3	2.04
Glass /FTO/TiO_2/ PA-$Cs_2AgBiBr_6$/Spiro/Au [21]	5.70	0.929	75	3.98
ITO/SnO_2/ $Cs_2AgBiBr_6$/Spiro/Au [35]	11.40	0.92	60.9	6.37
FTO/TiO_2/ $Cs_2AgBiBr_6$ /Spiro-OMeTAD/Ag (Our device)	7.97	0.988	86.52	6.81

4. Conclusion

In this study, the optoelectronic properties of a lead-free PCS based on $Cs_2AgBiBr_6$ was investigated using OghmaNano simulation software. A complete device structure composed of FTO/TiO_2/$Cs_2AgBiBr_6$/Spiro-OMeTAD/Ag was optimized by varying the layer thicknesses, doping concentration, and series resistance. The optimal configuration was achieved at 500 nm thick $Cs_2AgBiBr_6$ absorber material, leading to enhanced charge extraction and generation.

Under standard illumination (AM1.5G, 1000 W/m²) and temperature (300 K), the optimized cell exhibited Jsc of 7.97 mA/cm^2, Voc of 0.988 V, FF of 86.52%, and PCE of 6.81%. These findings emphasize the possibility of using double perovskite materials as environmentally friendly replacements for perovskites made with lead.

However, the relatively low current density, attributed to limited absorption in the near-infrared region, indicates that further improvements are required. Future work could focus on light management strategies, bandgap engineering, and especially the integration of tandem architectures to broaden the absorption spectrum and boost efficiency. This study provides a solid foundation for the continued progress of lead-free perovskite photovoltaic cells and underscores the importance of device engineering in unlocking their full potential.

As a perspective of this work, it would be interesting to explore advanced strategies to enhance near-infrared absorption, particularly by optimizing the design of the charge transport layers and introducing tandem structures based on $Cs_2AgBiBr_6$. These approaches could expand the spectral absorption range and maximize charge carrier generation and extraction. Additionally, the incorporation of light management techniques and bandgap engineering could provide new avenues for enhancing the stability and efficiency of these environmentally friendly devices.

References

[1] H. Y. F. Chen, W. T. Tang, J. J. He, M. S. Yin, Y. B. Wang, F. X. Xie, E. B. Bi, X. D. Yang, M. Grätzel and L. Y. Han, Nature, 2017, 550, 92–95; https://doi.org/10.1038/nature23877.
[2] Z. Shi, and al., ACS Nano, 2018, 12(2), 1462–1472; https://doi.org/10.1021/acsnano.7b07856.
[3] D. B. Mitzi, Synthesis, Structure, and Properties of Organic-Inorganic Perovskites and Related Materials, 2007, 48, 1–121; https://doi.org/10.1002/9780470166499.ch1.
[4] I. M. Asuo, Ambient-Processed Halide Perovskites for Photovoltaic and Optoelectronic Devices, University of Quebec, 2021; https://espace.inrs.ca/id/eprint/12468.
[5] A. Kojima, K. Teshima, Y. Shirai, T. Miyasaka, J. Am. Chem. Soc., 2009; https://doi.org/10.1021/ja809598r.
[6] J. P. Correa-Baena, M. Saliba, T. Buonassisi, M. Grätzel, A. Abate, W. Tress, A. Hagfeldt, Science, 2017, 358, 739; https://doi.org/10.1126/science.aam6323.
[7] S. Tang, Y. Deng, X. Zheng, Y. Bai, Y. Fang, Q. Dong, H. Wei, J. Huang, Adv. Energy Mater., 2017, 7, 1700302; https://doi.org/10.1002/aenm.201700302.
[8] D. Kumar, et al., ACS Omega, 2021, 6(49), 33240–52; https://doi.org/10.1021/acsomega.1c05333.
[9] Y. Zhao, et al., Matter, 2021, 4(6), 1801–31; https://doi.org/10.1016/j.matt.2021.03.009.
[10] G. Volonakis, et al., J. Phys. Chem. Lett., 2017, 8(4), 772–778; https://doi.org/10.1021/acs.jpclett.6b02682.
[11] H. C. Sansom, et al., J. Am. Chem. Soc., 2021, 143(10), 3983–3992; https://doi.org/10.1021/jacs.1c00495.
[12] P. Li, et al., Phys. Status Solidi A, 2019, 216(23), 1900567; https://doi.org/10.1002/pssa.201900567.
[13] S. E. Creutz, et al., Nano Lett., 2018, 18(2), 1118–1123; https://doi.org/10.1021/acs.nanolett.7b04659.
[14] E. T. McClure, et al., Chem. Mater., 2016, 28(5), 1348–1354; https://doi.org/10.1021/acs.chemmater.5b04231.
[15] E. T. McClure, et al., Chem. Mater., 2016, 28(5), 1348–1354; https://doi.org/10.1021/acs.chemmater.5b04231.

[16] M. R. Filip, S. Hillman, A. A. Haghighirad, H. J. Snaith, F. Giustino, J. Phys. Chem. Lett., 2016, 7, 2579; https://doi.org/10.1021/acs.jpclett.6b01041.
[17] W. Tress, M. T. Sirtl, Sol. RRL, 2021; https://doi.org/10.1002/solr.202100770.
[18] R. C. I. MacKenzie, C. G. Shuttle, M. L. Chabinyc, J. Nelson, Adv. Energy Mater., 2012, 2(6), 662–669; https://doi.org/10.1002/aenm.201100709.
[19] R. C. I. MacKenzie, T. Kirchartz, G. F. A. Dibb, J. Nelson, J. Phys. Chem. C, 2011, 115(19), 9806–9813; https://doi.org/10.1021/jp200234m.
[20] M. J. Yu, J. R. Yuan, X. H. Deng, J. Ovonic Res., 2025, 21(1), 1–18; https://doi.org/10.15251/JOR.2025.211.1.
[21] A. Ullah, et al., Results Phys., 2024; https://doi.org/10.1016/j.rinp.2024.107654.
[22] H. Menon, A. Amin, X. Duan, S. N. Vijayaraghavan, J. Wall, W. Xiang, K. A. Khawaja, F. Yan, Solar, 2024, 4, 222–23; https://doi.org/10.3390/solar4020010.
[23] A. Rajagopal, Z. Yang, S. B. Jo, I. L. Braly, P. W. Liang, H. W. Hillhouse, A. K. Y. Jen, Adv. Mater., 2017, 29, 1702140; https://doi.org/10.1002/adma.201702140.
[24] M. Atowar Rahman, SN Applied Sciences 3, 253, 2021; https://doi.org/10.1007/s42452-021-04267-3.
[25] Y. Bouachiba, A. Bouabellou, F. Hanini, F. Kermiche, A. Taabouche, K. Boukheddaden, Mater Sci-Poland 32, 1–6, 2014; https://doi.org/10.2478/s13536-013-0147-z.
[26] M. S. S. Basyoni and al., IEEE Access 9, 130221–130232, 2021; https://doi.org/10.1109/ACCESS.2021.3114383.
[27] A. Bag, R. Radhakrishnan, R. Nekovei, R. Jeyakumar, Sol. Energy 196, 177, 2020; https://doi.org/10.1016/j.solener.2019.12.014.
[28] L. M. Pazos-Outón, T. P. Xiao, J. Yablonovitch, , Phys. Chem. Lett. 9, 1703–1711, 2018; https://doi.org/10.1021/acs.jpclett.7b03054.
[29] Otmani Fatima Zohra, “Simulation et optimisation des cellules solaires de type : simple et tandem à base de pérovskite $CH_3NH_3PbI_3$”, University Abou-Bekrbelkaid-TLEMCEN, ALGERIA, 2025.
[30] F. Otmani, N. Bachir, A. Merad, Journal of Ovonic Research. 21(1), 95–107, 2025; https://doi.org/10.15251/JOR.2025.211.95.
[31] M. Sadiq et al., Materials Research Express 8, Art. no. 095507, 2021; https://doi.org/10.1088/2053-1591/ac2377.
[32] L. Sims, U. Hörmann, R. Hanfland, R. C. I. MacKenzie, F. R. Kogler, R. Steim, P. Schilinsky, Organic electronics, 15, 2862–2867, 2014; https://doi.org/10.1016/j.orgel.2014.08.010.
[33] Y. Liu, R. C. I. MacKenzie, B. Xu, Y. Gao, M. Gimeno-Fabra, D. Grant, P. H. M. van Loosdrecht, T. Wenjing, Journal of Materials Chemistry C 3, 12260–12266, 2015; https://doi.org/10.1039/C5TC02678D.
[34] B. Wang et al., Sol. RRL 4(7), 2000166, 2020; https://doi.org/10.1002/solr.202000166.
[35] D. Zhang et al., Adv. Funct. Mater. 32(27), 2200174, 2022; https://doi.org/10.1002/adfm.202200174.